RSC Advances

PAPER

View Article Online
View Journal | View Issue

Cite this: *RSC Adv.*, 2026, **16**, 23848

Effect of Si additions on the mechanical and electrochemical behavior of the as-casted Ti-15Mo alloy in simulated body fluid for biomedical applications

Ashraf Bakkar,[a] Mohamed M. El-Sayed Seleman,*[b] Sabbah Ataya,[c] Hagar A. Reyad,[d] Khaled M. Ibrahim[e] and Hayam A. Aly[e]

Titanium (Ti) and its alloys are preferred biomaterials for orthopedic and dental implants due to their excellent biocompatibility and corrosion resistance. However, the development of non-toxic β-Ti alloys with low elastic modulus, high strength, and superior corrosion resistance remains a key challenge for long-term implant applications. The Ti-15Mo alloy is a promising candidate due to its good biocompatibility and mechanical properties. This study investigates the influence of silicon additions (0–2 wt%) on the microstructure, mechanical properties, and corrosion behavior of as-cast Ti-15Mo-*x*Si alloys for biomedical applications. The corrosion behavior was investigated by potentiodynamic polarization and electrochemical impedance spectroscopy (EIS) at 37 °C in simulated body fluid (SBF). Moreover, the passive films formed on the surfaces of the alloys were examined using X-ray photoelectron spectroscopy analysis (XPS). The results indicated that Si additions refined the grain size and improved the mechanical properties. All alloys spontaneously formed a stable passive oxide layer. Crucially, the corrosion resistance improved systematically with Si content, as evidenced by a nobler open-circuit potential, a lower corrosion current density (reaching ~1.03×10^{-7} A cm^{-2} for the 2 wt% Si alloy), and a higher passive film resistance. XPS confirmed that the passive film is primarily composed of TiO_2, with the superior performance of the 2 wt% Si alloy attributed to a denser, more compact oxide layer enriched with protective silicon oxides. The Ti-15Mo-2Si alloy, combining high strength and exceptional corrosion resistance, emerges as a highly promising candidate for load-bearing surgical implants.

Received 4th March 2026
Accepted 25th April 2026

DOI: 10.1039/d6ra01849a

rsc.li/rsc-advances

1. Introduction

Pure titanium (Ti) and titanium alloys are used in medical fields such as orthopedics,[1–5] bone prosthesis,[6] and dentistry implant applications.[7–9] These materials are characterized by their formability, large specific strength, low elastic modulus, high mechanical properties, high corrosion resistance, and biocompatibility.[10–12] β-phase Ti alloys exhibit higher mechanical properties and lower elastic modulus compared to those with an α-phase.[1,13] Alloying elements are added to enhance the mechanical properties, decrease the elastic modulus, or increase the corrosion resistance of Ti alloys.[2] Aluminum (Al)[14] and vanadium(v)[15,16] as alloying elements provide a remarkable improvement in the mechanical properties and corrosion resistance of Ti-alloys.[1,7] However, when these alloying elements exceed a threshold limit in the Ti alloys implemented in biomedical applications, they may cause osteomalacia,[17] peripheral neuropathy,[18] and Alzheimer's disease.[1] Other alloying elements, such as niobium (Nb), tantalum (Ta), zirconium (Zr), molybdenum (Mo) and silicon (Si), are considered as non-toxic and effective β-phase stabilizers. The addition of Mo to Ti alloys improves the corrosion resistance[19] and the mechanical properties,[20,21] while reducing the modulus of elasticity.[22]

Beyond traditional alloying, recent advancements have explored innovative surface and microstructural engineering strategies to further enhance the functional performance of Ti-based biomaterials. For instance, Liu *et al.*[23] demonstrated that

[a]*Department of Civil and Environmental Engineering, College of Engineering and Computers, Umm Al-Qura University, Al-Lith 28425, Saudi Arabia. E-mail: atbakkar@uqu.edu.sa*

[b]*Department of Metallurgical and Materials Engineering, Faculty of Petroleum and Mining Engineering, Suez University, Suez 43221, Egypt. E-mail: mohamed.elnagar@suezuniv.edu.eg*

[c]*Department of Mechanical Engineering, College of Engineering, Imam Mohammad Ibn Saud Islamic University (IMSIU), Riyadh 11432, Saudi Arabia. E-mail: smataya@imamu.edu.sa*

[d]*Arabian Steel Industries, Suez 43552, Egypt. E-mail: H.reyad@arabiansteel.net*

[e]*Central Metallurgical Research and Development Institute (CMRDI), P.O. Box 87, Helwan 11421, Egypt. E-mail: hayam.abokhasha79@yahoo.com; khaledabouelela@yahoo.com*

incorporating bioactive elements like zinc (Zn) into micro-arc oxidation coatings can significantly improve the long-term antibacterial efficacy and biofilm inhibition of Ti-alloys. Similarly, Ouyang *et al.*[24] showed that regulating multiscale microstructures through laser shock peening can optimize the balance between surface damage resistance and overall mechanical integrity by creating gradient grain structures. These studies underscore the importance of microstructural and surface refinement in tailoring Ti alloys for advanced biomedical applications, complementing the bulk alloy design approach adopted in the present work.

Moreover, Si addition to Ti-alloys increases the fluidity[25] and the creep resistance at high temperatures,[26,27] but simultaneously reduces the ductility.[28] Si contents have also been reported to improve the corrosion resistance.[29] The Ti alloys designed for biomedical applications, particularly orthopedic implants, should exhibit excellent corrosion resistance.[30] Electrochemical dissolution accelerated by erosion of Ti alloys used for load-bearing implants may generate debris.[31] When these accumulated debris are found around the human tissues or dissolved in the human blood, they can result in damages and adverse effects on the cell tissue that may include carcinogenic potential.[31,32]

Oliveira and Guastaldi[10] examined the impact of different Mo content on the corrosion behavior of Ti-*x*Mo alloy. The Mo contents ranged from 4 to 20 wt%. The Ti-*x*Mo alloys were produced in an arc melting furnace under an ultra-pure argon atmosphere. These alloys were tested in Na_2SO_4 and Ringer's electrolytes. They reported that the open-circuit potential profiles of the tested Ti-*x*Mo alloys in both electrolytes were relatively similar, indicating the formation of a passive oxide film. Furthermore, they concluded that Mo improved the corrosion resistance in Na_2SO_4 due to the formation of the anodic oxide film.

Sutowo *et al.*[13] investigated the influence of manganese (Mn) addition, in the range of 0–12 wt%, on the corrosion behavior and mechanical performance of Ti-9Mo-6Nb-*x*Mn alloys produced in a vacuum arc furnace. They found that the corrosion rate in Ringer's solution decreases with increasing Mn content. The authors ascribed improving the corrosion resistance to the beneficial effect of Mn on stabilizing the titanium oxide film formed that gets more stable and denser with increasing Mn content. Ghica *et al.*[19] investigated the effect of adding tungsten (*W*), in the range of 7–10 wt%, to Ti-19Mo alloy on its corrosion resistance in simulated body fluid (SBF) electrolyte. The Ti-19Mo-7W alloy exhibits the lowest corrosion rate. Hulka *et al.*[33] studied the corrosion resistance of Ti-*x*Ta alloys (x = 5, 15, and 25 wt% Ta) produced in an induction furnace using argon gas. The alloys demonstrate a higher corrosion resistance in SBF electrolyte due to the formation of a passive film of TiO_2-Ta_2O_5. Xu *et al.*[34] investigated the corrosion behavior of Ti-12Mo alloy in four different electrolytes: saline solution (SS), SBF, phosphate-buffered saline (PBS), and modified Fusayama artificial saliva (FAS) at a temperature of 37 °C. The authors compared the results with that of the Ti-6Al-4V alloy. They found that the Ti-12Mo alloy shows lower corrosion current density and the higher pitting resistance in the four different electrolytes owing to the formation of a protective passive film of TiO_2-MoO_3, which was more stable. Jiang *et al.*[35] studied the effect of different Si content on the corrosion resistance of Ti-*x*Si alloys. The Si contents were 2, 4, 6, 8.5, and 11 wt%. They reported that Ti-*x*Si alloys exhibit higher corrosion resistance in acidic 0.1M Na_2SO_4 solution (acidified with H_2SO_4) owing to the formation of TiO_2-SiO_2 passive film.

This study examined the influence of silicon additions (0, 0.5, 1, 1.5, and 2 wt%) on the microstructure, mechanical characteristics, and corrosion behaviour of Ti-15Mo-*x*Si alloys to assess their potential application as biomedical materials. The corrosion behaviour of Ti-15Mo-*x*Si was investigated based on open-circuit potential (OCP) measurements, electrochemical impedance spectroscopy (EIS), and X-ray photoelectron spectroscopy (XPS) examination for the passive films formed on the surfaces of the alloys.

2 Materials and methods

Highly pure metallic elements Ti, Mo, and Si were used to prepare Ti-15 wt% Mo-*x*Si alloys, where x = 0.5, 1, 1.5, and 2 wt%. The starting materials were supplied by Nilaco Corporation, Japan, in the form of irregular small metallic pieces with a purity of ≥99.96% for each metal. The Ti-15Mo-*x*Si alloys were fabricated by vacuum arc remelting (VAR) using a furnace (model ARCAST 800A, USA) under a high-purity argon atmosphere. To ensure composition homogeneity, the melt was subjected to magnetic stirring before being cast into a water-cooled copper mold to achieve rapid solidification. This rapid solidification is essential for retaining the metastable β-Ti phase at room temperature and preventing the formation of coarse microstructures or unwanted intermetallic phases.[36,37] The as-cast alloys were obtained in the form of disc-shaped ingots with a diameter of approximately 50 mm and a height of about 14 mm, weighing approximately 100 g per ingot. The ingots were sound, with smooth surfaces and free from visible porosity or cracking defects. The actual chemical composition of the as-cast Ti-15Mo-*x*Si alloys was verified using optical emission spectrometry (Foundry-Master Pro). The results are summarized in Table 1, confirming that the final compositions are in close agreement with the nominal values, with slight deviations within the typical range for arc-melted alloys.

The as-cast Ti-15Mo-Si alloys were sectioned and machined into specimens for characterization. For microstructural analysis, the specimens were ground with progressively finer SiC papers up to 2400 grit, polished with diamond suspensions, and

Table 1 Actual chemical composition (wt%) of the as-cast Ti-15Mo-*x*Si alloys

Alloy	Mo	Si	Mn	Fe	Ti
Ti-15Mo	15.03	0.00	0.020	0.003	Bal.
Ti-15Mo-0.5Si	15.01	0.52	0.021	0.003	Bal.
Ti-15Mo-1.0Si	15.10	1.01	0.022	0.004	Bal.
Ti-15Mo-1.5Si	15.12	1.52	0.023	0.006	Bal.
Ti-15Mo-2.0Si	15.09	2.03	0.023	0.011	Bal.

finally with a silica colloidal suspension. The polished surfaces were then chemically etched with Kroll's reagent, consisting of a 2 : 4 : 94 (by volume) mixture of 40% hydrofluoric acid, 69% nitric acid, and distilled water. The microstructure of the prepared samples was characterized using an optical microscope (OM; BX41M-LED, Olympus, Tokyo, Japan). For each alloy composition, three separate specimens were examined, and at least three to five non-overlapping optical micrographs were captured per specimen. The analyzed area per micrograph was approximately 1.72 mm × 1.28 mm (2.20 mm^2), providing a statistically representative grain count for all alloys. Grain size analysis was performed using the linear intercept method according to ASTM E112. Furthermore, the microstructural details and elemental distributions were investigated using a field emission scanning electron microscope (FESEM; FEI Quanta 250 FEG, USA) equipped with an energy-dispersive X-ray spectroscopy (EDS) system, operated at an accelerating voltage of 20 kV. Phase identification was performed by X-ray diffraction (XRD, model Shimadzu XRD-6100, Japan) using Cu-Kα radiation. XRD patterns were recorded in the 2θ range of 20° to 100° with a scanning speed of 1° min^{-1}. The mechanical properties of hardness and compressive strength were evaluated using two distinct testing apparatuses. Compression test specimens were machined from the as-cast ingots using a wire electrical discharge machine (EDM) into cylindrical samples of 6 mm in diameter and 12 mm in height, according to ASTM E9 standards. For each alloy composition, three cylindrical specimens were tested. The tests were conducted at room temperature using a universal testing machine (WDW-300, Jinan Precision Testing Equipment Co., Ltd) with a constant crosshead speed of 0.2 mm min^{-1}. Vickers hardness measurements were obtained on a universal hardness tester (INNOVATEST NEMESIS 9104) with a 2 kg load held for a dwell period of 15 s. For each alloy composition, ten indentations were made at different locations across the sample surface.

To study the corrosion performance of Ti-15Mo-*x*Si alloys in SBF solution at 37 ± 1 °C *via* free corrosion potential, namely open circuit potential (OCP) measurement, and potentiodynamic polarization, a conventional three-electrode cell was used. In this setup, the specimen served as the working electrode, a platinum wire was acted as the counter electrode, and a saturated calomel electrode (SCE) functioned as the reference electrode. For monitoring the OCP, the specimen was exposed to the SBF solution for 1 h, by which time a quasi-stable potential was obtained. Then, with the reference to SCE, the potentiodynamic polarization diagrams were recorded using a PC-controlled potentio/galvanostat "model Auto lab PGSTAT 30". The potential was scanned from about −300 mV *vs.* SCE, more negative than OCP, up to 700 mV *vs.* SCE with a potential step of 1 mV and a scan rate of 1 mV s^{-1}. The corrosion potential (E_{corr}) and the corrosion current (I_{corr}) were determined by extrapolation of cathodic and anodic Tafel lines. The measurements for electrochemical impedance spectroscopy (EIS) were conducted after 1 h of free immersion. The EIS measurements were taken in the frequency range of 100 kHz to 0.1 Hz, using a 0.01 V amplitude voltage signal at a temperature of 37 °C.

The composition of the formed oxide layer was examined by X-ray photoelectron spectroscopy (XPS, Thermo Fisher Scientific™ K-Alpha, USA). The system featured a monochromatic X-ray source (Al Kα radiation) that was operated with a 400 μm spot size. Measurements were conducted in an ultra-high vacuum (10^{-9} mbar). Survey spectra were acquired across a range of −10 and 1350 eV, while high-resolution narrow-spectrum scan of 50 eV pass energy. To complement the chemical analysis, the surface morphology of the passive films formed after the electrochemical tests was characterized using the same FESEM system to evaluate the compactness and uniformity of the oxide layers.

3 Results and discussion

3.1 XRD and microstructures analysis

The microstructural phase composition of the Ti-15 wt% Mo-*x*Si alloy system was systematically investigated using XRD across the 2θ range of 20 to 100°. The resultant patterns are presented in Fig. 1. Using a water-cooled copper hearth, all the cast alloys across the entire compositional range from 0.0 to 2.0 wt% Si additions were fabricated by VAR, a technique that imposes rapid solidification and encourages solid-state phase retention. The XRD confirms a uniform phase composition was observed. All samples were identified exclusively as the body-centered cubic (β-Ti) phase, being entirely free of the typical hexagonal close-packed (α-Ti) phase or any deleterious intermetallic compounds. This clear finding validates the effectiveness of the chosen alloying scheme, confirming that Mo and Si are strong β-stabilizers that keep this high-temperature phase stable at room temperature[36,37] Furthermore, a clear correlation is observed, where the intensity of the β-Ti phase increases significantly with higher silicon content across the range of 0.5

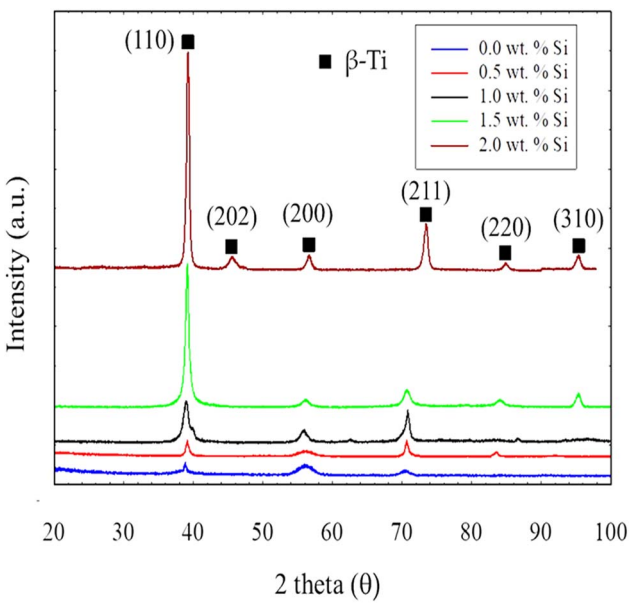

Fig. 1 XRD phases patterns for all compositions within the Ti-15Mo-*x*Si processed alloy systems.

Table 2 XRD peak position (2θ), maximum intensity, interplanar spacing (d), and calculated lattice parameter (a) for Ti-15Mo-xSi alloys

Sample (wt% Si)	Peak position (2θ)	Max intensity (counts)	d (110) (Å)	Lattice parameter (a) (Å)
Ti-15Mo	38.8°	179.3	2.319	3.279
Ti-15Mo-0.5Si	39.0°	414.5	2.307	3.262
Ti-15Mo-1.0Si	39.2°	1115.9	2.296	3.247
Ti-15Mo-1.5Si	39.4°	3685.5	2.285	3.231
Ti-15Mo-2.0Si	39.5°	5584.9	2.279	3.224

to 2.0 wt%. This rise in intensity is interpreted as a direct consequence of the non-equilibrium solidification conditions established during the production process. The fast-cooling rate facilitates the complete dissolution of the primary elements into the crystalline lattice, thereby maximizing the resultant volume fraction and the crystalline perfection of the β-phase solid solution. Similar phenomena have been observed in metastable β-Ti alloys, where rapid cooling from above the β-transus temperature effectively suppresses the precipitation of secondary phases and retains a high-quality β-matrix. This interpretation is consistent with the findings of Terynková *et al.*[38] who demonstrated that rapid cooling in Ti-15Mo alloys effectively retains the β-phase in a solution-treated state. Furthermore, Gupta *et al.*[39] highlighted that accelerated cooling rates directly influence the lattice parameters and crystalline order in titanium systems. Additionally, the recent study by Shang *et al.*[40] on metastable β-titanium confirmed that high cooling rates (up to 400 °C min^{-1}) are crucial for maintaining a high-volume fraction of the β-matrix and achieving superior structural homogeneity. To provide a quantitative basis for these structural observations, the maximum intensity and the lattice parameter (a) for the (110) β-peak were determined for all investigated alloys. The results are summarized in Table 2.

As demonstrated in Table 2, the maximum intensity of the β-Ti phase increases dramatically (nearly 30-fold) with the addition of 2.0 wt% Si. This substantial rise in intensity, coupled with the systematic contraction of the lattice parameter (a) from 3.279 Å to 3.224 Å, confirms that Si atoms are successfully incorporated into the substitutional sites of the BCC lattice. The perceived lower intensity of the binary Ti-15Mo alloy in Fig. 1 is a relative effect due to the massive enhancement in crystalline perfection and X-ray constructive interference provided by Si stabilization under rapid solidification conditions. These quantitative findings definitively confirm the high crystallinity of the produced alloys and align with the established role of Si as a potent β-stabilizer.

The microstructural evolution of the Ti-15Mo-xSi alloy system was critically dependent on the its Si content, which was systematically varied between all cast specimens displayed a homogeneous, single-phase β-Ti microstructure, indicating the structural stability of the high-temperature phase at room temperature throughout the compositions investigated. This microscopic structure is consistent with the initial design of these alloys produced by adding 15% Mo. This addition stabilizes the titanium in the beta phase,[41] and the presence of Si also acts as a beta-stabilizer.[42] This microstructure agrees with the results obtained in Fig. 1 (XRD-phase analysis results). Fig. 2 displays the grain structure and the grain size variation of the Ti-15Mo cast alloy and the alloys produced with various Si additions. A significant reduction in grain size is observed even at 0.5% Si (Fig. 2b and c), compared to the base alloy (Fig. 2a and b) and this reduction continues to increase with higher Si additions up to 2% (Fig. 2c and d). These results indicate that Si acts as an effective grain refiner; which positively influences the mechanical properties.[37] It can be concluded that across the Si range studied (0.0–2.0 wt%), the average grain size decreased substantially, from approximately 508 μm to 112 μm, demonstrating a clear trend of refinement for the Ti-15Mo-xSi alloy system.

To further investigate the microstructural features and address the potential formation of Si-based intermetallics, SEM observations were conducted (Fig. 3). For the Ti-15Mo alloy (Fig. 3a), a clean β-matrix with coarse grains is evident. In contrast, the Ti-15Mo-2Si alloy (Fig. 3b) exhibits a significantly refined grain structure. Although the Ti-Si equilibrium phase diagram suggests the precipitation of silicide such as Ti_5Si_3 or Ti_3Si,[43] no distinct coarse intermetallic particles were observed at the SEM resolution. This absence in both XRD and SEM suggests that the Si remains largely in solid solution or forms sub-microscopic, finely dispersed precipitates due to the high cooling rates associated with the VAR process. Consequently, the observed grain refinement from 508 μm to 112 μm is attributed to the high growth restriction factor of Si, which induces constitutional supercooling and suppresses grain growth during solidification.

3.2. Mechanical properties characterization

Mechanical properties of Ti alloys are governed by their chemical composition, phase structure, and grain size. The mechanical properties of the Ti-15Mo-xSi alloys were evaluated through hardness and compression testing. Fig. 4a presents the compressive stress–strain curves of the Ti-15Mo-xSi alloys with different Si contents (0, 0.5, 1, 1.5, and 2 wt%). All alloys exhibit typical ductile behavior, with a linear elastic region followed by plastic deformation up to failure. The curves demonstrate that increasing Si content systematically enhances the overall compressive strength and ductility of the alloys. Fig. 4b displays the average hardness and compressive strength data for the Ti-15Mo-xSi alloy series. The data show a systematic increase in hardness across the Si range (0.0–2 wt%). The Ti-15Mo-2Si system has the highest hardness value of 443 Hv. This improvement in hardness behavior attributed to the grain

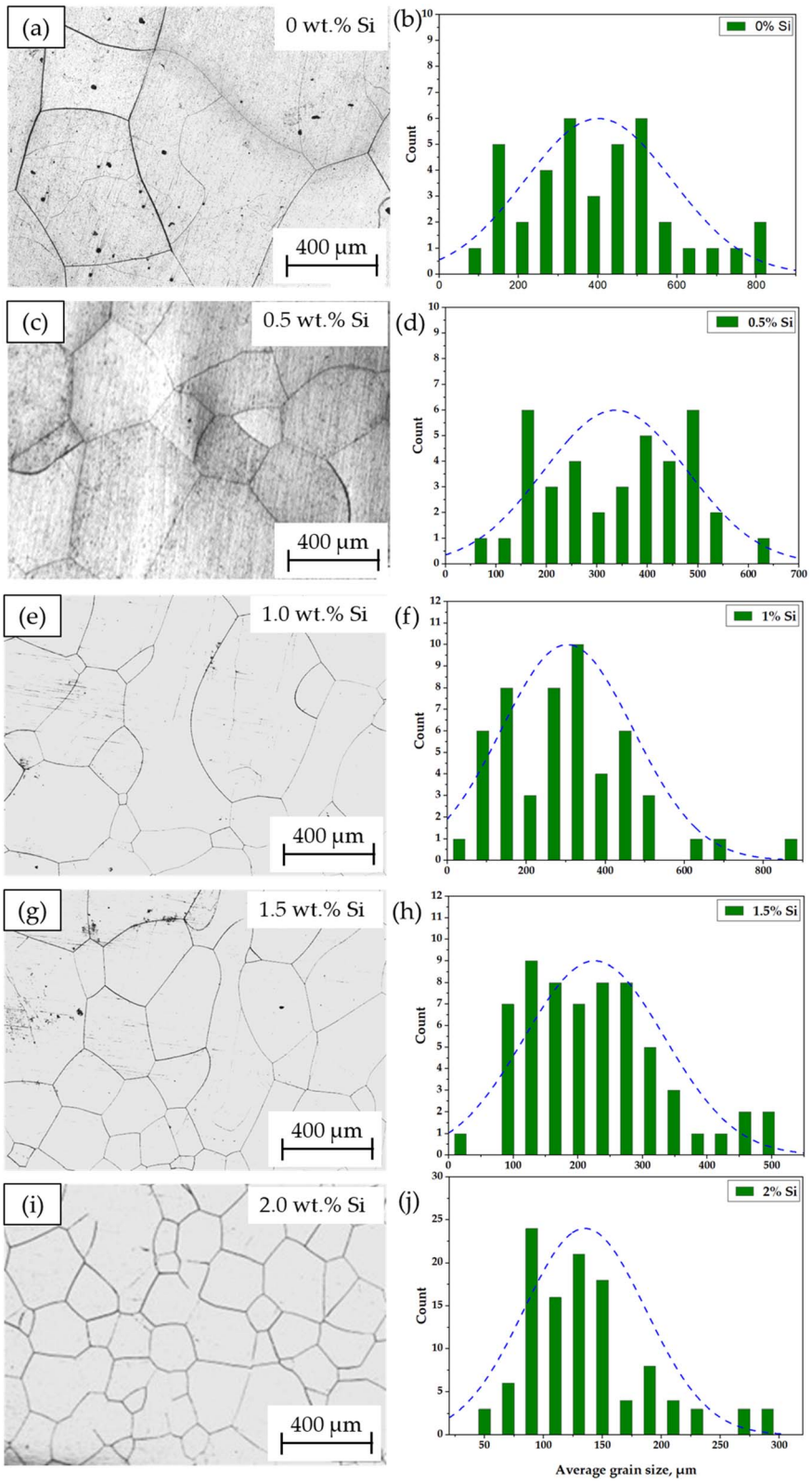

Fig. 2 OM micrographs illustrating the microstructure (a, c, e, g and i) and associated grain size measurements (b, d, f, h and j) across the Ti-15Mo-*x*Si composition range.

refinement promoted by higher Si content. A similar strengthening effect is observed under compression. For instance, the compressive strength improves from 1240 ± 34 MPa for the binary alloy (Ti-15Mo) to 1679 ± 23 MPa for the 2 wt% Si alloy system (Ti-15Mo-2Si). This trend is consistent with findings in the literature.[26] Furthermore, published studies on β-Ti alloys,

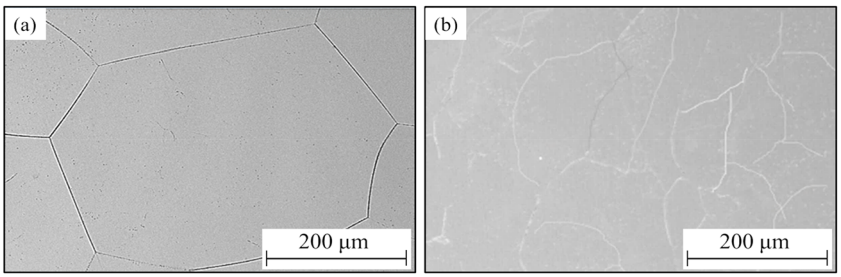

Fig. 3 SEM micrographs illustrating the microstructural features of (a) Ti-15Mo base alloy and (b) Ti-15Mo-2Si alloy.

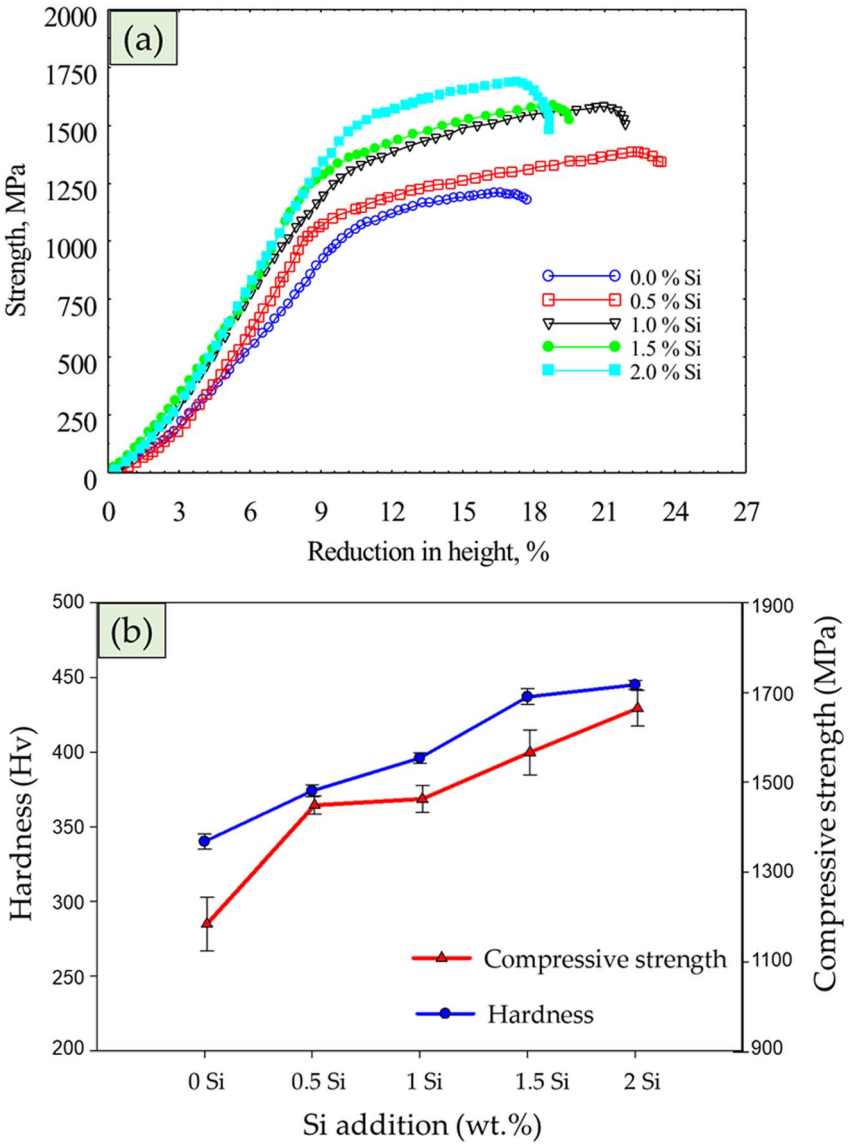

Fig. 4 (a) Compressive stress–strain curves and (b) average values of hardness and compressive strength for all produced Ti-15Mo-*x*Si alloys.

such as those by Kunčická *et al.*[32] reported that β-Ti alloys had ultimate tensile strength ranging from 600 to 1100 MPa.

To evaluate the competitive standing of the developed Ti-15Mo-*x*Si alloys, their properties were compared with the conventional Ti-6Al-4V benchmark. While wrought Ti-6Al-4V typically exhibits an ultimate tensile strength of 884–965 MPa depending on the processing conditions and surface treatments like laser shock peening,[24] our as-cast Ti-15Mo-2Si alloy demonstrates a significantly higher compressive strength of 1679 MPa. This robust resistance to deformation is further

contextualized by a recent study on the microstructural tailoring of Ti-6Al-4V, which emphasize that property enhancement is highly dependent on grain refinement and phase distribution.[44] Given that orthopedic and dental implants are primarily subjected to compressive physiological stresses, the superior axial strength and refined β-matrix of the Ti-15Mo-*x*Si system make it a highly promising candidate for long-term load-bearing applications.

3.3. Open circuit potential and polarization studies

Fig. 5 shows the time–variation profile of the open circuit potential "OCP" values for the investigated alloys during 1 h of immersion in SBF solution at 37 °C. All alloys exhibited a similar behavior; the OCP shifted significantly toward more positive (nobler) potentials during the first twenty minutes. Thereafter, the OCP increased slowly and moderately to stabilize at a quasi-stationary potential, indicating formation of a stable passive film on the alloy surfaces.

The results presented in Fig. 4 and Table 1 indicate that all investigated Ti-Mo-*x*Si alloys show the same tendency to spontaneously form a passive film. The addition of Si in different weight percentages enhances the formed protective passive oxide film. Similar electrochemical behavior has been reported for Ti-Mo alloys in Ringer's solution[41] and in PBS solution.[45] The OCP of the Ti-15Mo alloy shifted toward more noble values upon the addition of Si. As the Si content increased, the OCP became significantly nobler; specifically, the 2 wt% Si alloy exhibited a potential approximately +176 mV more noble than that of the Si-free alloy.

Fig. 6 illustrates the potentiodynamic polarization diagrams of Si-free and Si-containing Ti-15Mo alloys in SBF solution at 37 °C. The drawn curves show similar behavior related to passive characteristics and indicate the formation of a passive film on the surfaces of all the produced Ti-Mo-*x*Si alloys, that suggest the Ti-Mo-*x*Si alloys can be passivated in human body environment. These results are in good agreement with previous studies that dealt with different corrosive solutions

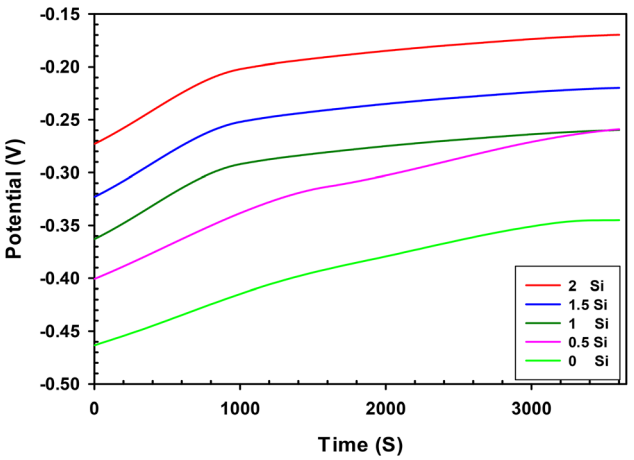

Fig. 5 Open-circuit potential (OCP) evolution as a function of immersion time for Ti-15Mo-*x*Si alloys in SBF at 37 °C (Si contents: 0, 0.5, 1, 2 wt%).

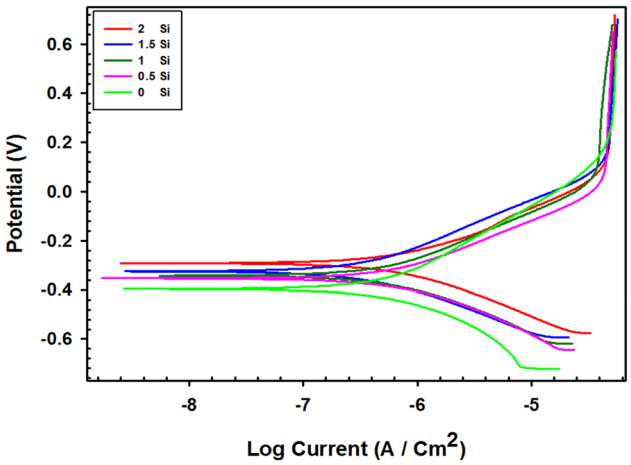

Fig. 6 Representative potentiodynamic polarization plots showing the corrosion behavior of Ti-15Mo-*x*Si alloys with varying Si content (0–2 wt%) in a 37 °C SBF solution.

belonging to similar simulated physiological media.[46] The results demonstrate that the polarization curves for the Si-containing alloys shifted in the noble direction compared to that of the Si-free alloy. For a clearer comparison, the corrosion potential (E_{corr}), and the corrosion current (I_{corr}), as well as the OCP values, are listed in Table 3. Notably, the E_{corr} values determined by the polarization curves are lower (less noble) than the OCP values measured *via* free immersion. This can be attributed to the partial destroying effect on the passive film by the reduction reactions during the cathodic polarization sweep. Contu[47] reported the occurrence of both oxygen reduction and hydrogen evolution reactions during the cathodic polarization sweep of Ti in FBS solution.

Tracing the polarization curves (Fig. 6) reveals that the cathodic polarization curves displayed by the alloys seemed to be similar with no observable difference in the cathodic branches. This suggests occurrence of the similar cathodic reaction on the surfaces of alloys. Also, the cathodic Tafel slope (β_c) for all alloys recorded a high value (greater than 118 mV dec^{-1}), likely indicating the presence of a passive or surface-modified film on the alloys.[47] Starting from the E_{corr}, the alloys initially demonstrated an anodic behavior similar to active metals. That is, as the electrode potential increased, the dissolution rate increased and hence the current increased exponentially, and the corrosion of the alloys followed the typical Tafel behavior. Thereafter, the increasing rate of the current density diminished to a very low value, indicating the inhibiting of metallic dissolution of the alloys due to formation of a passive or surface-modified protective film, and the current density remained approximately constant independent of potential over a considerable potential region. This constant current is termed the passive current density (I_{pass}), and this region is specified as the passivation region. The alloys reached that well-defined passivation region at the potential range of 0.0–100 mV_{SCE} and displayed I_{pass} within the same order of magnitude ranging between 60 and 80 μA cm^{-2}.

Table 3 Electrochemical parameters derived from the potentiodynamic polarization analysis of the Ti-15Mo-*x*Si alloys in SBF at 37 °C

Ti-15Mo-*x*Si alloys	OCP (mV)	E_{corr} (mV)	I_{corr} (A cm^{-2})	β_c (mV dec^{-1})	β_a (mV dec^{-1})
0.0 %Si	−348	−396	1.45×10^{-7}	−187	198
0.5 %Si	−270	−354	1.31×10^{-7}	−153	182
1.0 %Si	−271	−342	1.22×10^{-7}	−163	193
1.5 %Si	−235	−325	1.08×10^{-7}	−156	196
2.0 %Si	−172	−292	1.03×10^{-7}	−166	133

Eventually, it can be stated from the potentiodynamic polarization behavior that the alloys studied had essentially a passivation behavior, and the Si-contained Ti-Mo alloys showed nobler E_{corr} and this nobility increased with increasing the Si content. The I_{corr} was reduced in Si-containing alloys, showing a somewhat consistent trend with increasing Si content. Such behavior aligns with the results previously reported on the corrosion behavior of Ti-20 Mo-*x*Si ($x = 0.5$, 0.75, 1.0 wt %Si) by Baltatu *et al.*[46] It is worth mentioning that the I_{corr} determined by extrapolation of Tafel lines is not accurate due to the partial deterioration of passive film during the cathodic sweep and re-formation of the passive film on the anodic polarization. Hence, the I_{corr} can be used for qualitative evaluation of the impact of Si on the corrosion resistance of Ti-Mo alloys.[45]

3.4 Electrochemical impedance spectroscopic "EIS" studies

3.4.1 Selection of the equivalent circuit. The previous electrochemical behavior studies, using potentiodynamic polarization and EIS techniques, postulated that the Ti alloys form a single passive film after immersion for short times in the solutions simulating the physiological media. This formation of a stable single passive film is approved by the results of the potentiodynamic polarization of Ti-15Mo-*x*Si alloys studied in this work; where the polarization curves revealed a stability of passive current over a considerable range of anodic potential, as shown in the explanation of Fig. 6.

The following EIS results revealed a convenient fitting of all data arisen from assuming the simple "$R_s(QR_p)$" circuit represented in Fig. 6, where R_s is the solution resistance, R_p is the parallel film resistance, and Q is a constant phase element "CPE" which takes into account the capacitive behavior of the film. The $R_s(QR_p)$ equivalent circuit model is postulated to fit EIS behavior of Ti-Mo alloys.[10,45,48] Titanium passivates in aqueous solutions, even containing Cl ions, forming TiO_2. The mechanism of Ti passivation is attributed to the rapid hydrolysis of $TiCl_4$, if formed by adsorption of Cl anions, forming TiO_2 passive film.[10,48,49] Mo stabilizes the TiO_2 passive film forming a much more corrosion resistant passive film of TiO_2 and MoO_3 (ref. 10 and 49).

3.4.2 Presentation of EIS results through bode diagrams. Fig. 7a reveals that all Nyquist plots displayed incomplete semicircles that represent the capacitive response of the passive film on the surface.[46] The impedance value increased with Si content and the maximum impedance was recorded for 2 wt % Si Alloy. Fig. 7b and c present the Bode magnitude and phase angle diagrams, respectively, for the four Ti-15Mo-*x*Si alloys studied in the SBF solution. The alloys containing Si, depicted an obviously capacitive behavior, representative of passive metals, which is recognized from the phase angle approaching −90° from medium to low frequencies.[45] The 2 wt% Si alloy was distinguished by a highly capacitive behavior, typical of passive metals, that was characterized by the highest phase angle approaching −80° from medium to low frequencies. This suggests that a much more stable film is formed on 2 wt% Si alloy compared to other Si-containing alloys tested in the SBF solution.

Table 4 displays the resistance, capacitance, and n values of the passive film, arisen out adjusting the experimental data using the "$R_s(QR_p)$ equivalent circuit model" represented in Fig. 8. The film resistance "R_P" possesses the same order of magnitude (10^5 Ω cm^{-2}) reported by other studies on some Ti-Mo alloys.[10,46,48] However, the R_P increased with Si content and reached its highest value, 9.58×10^5 Ω cm^{-2}, for Ti-15Mo-2Si alloy, indicating that the passive oxide film formed spontaneously on Ti-Mo alloys became more resistant with Si addition. The n values, closely to 1, indicated that the behavior of such passive oxide film approached that of an ideal capacitor.[50]

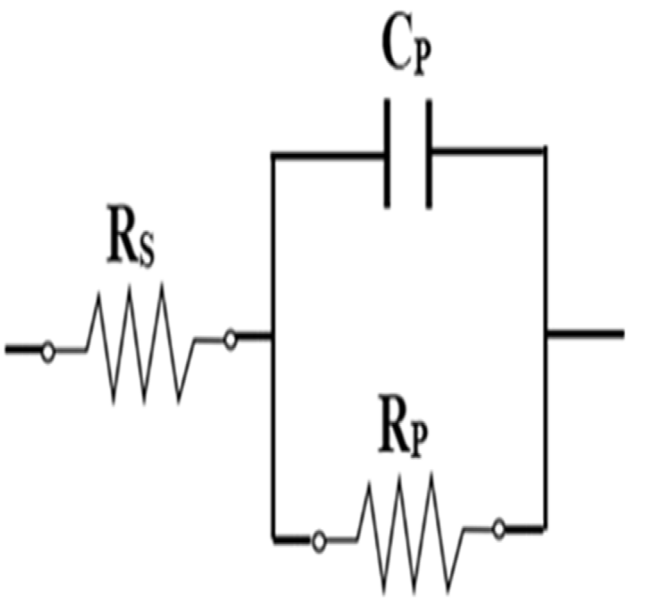

Fig. 7 Equivalent electrical circuit used for fitting the EIS experimental results obtained in SBF solution at 37 °C.

Table 4 Electrical parameters obtained from the fitting of the impedance data measured at OCP for Ti-15 Mo-*x* Si alloys using the "$R_s(QR_p)$" equivalent circuit

Alloy containing *x* wt% Si	R_p (Ω)	R_s (Ω)	*Q*, CPE (μF)	*n*
1.0 wt.%Si	1.679×10^5	538	9.48	0.89
0.5 wt.%Si	2.001×10^5	562	7.92	0.88
1.0 wt.%Si	2.220×10^5	572	7.15	0.88
1.5 wt.%Si	3.698×10^5	536	4.30	0.86
2.0 wt.%Si	9.580×10^5	553	1.66	0.90

It can be stated that the corrosion results revealed that the formed passive film on Ti-15Mo-*x*Si alloys surface is highly corrosion resistant. With increase in Si content, the passive film becomes more compact and improves the corrosion resistance, to be the highest at 2 wt% Si.

3.5. X-ray photoelectron spectroscopy (XPS) spectra

Following corrosion testing, XPS was employed to characterize the composition of the passive films formed on the surfaces of the 0, 1, and 2 wt% Si alloys (Fig. 9 and 10). This analysis aimed to provide more precise information about the surface chemistry. The wide-energy region of XPS spectra highlights the peaks corresponding to Ti 2p, Mo 3d, O 1s, and C 1s for all alloys, with Si 2p peaks appearing in the silicon-containing samples, as shown in Fig. 9. Remarkably, the XPS spectrum for the 2 wt% Si alloy displayed more pronounced Si 2p peaks compared to the 0 wt% Si alloy. The C 1s peak was not considered in the analysis because it originated from inevitable surface contamination due to the absorption of ambient air.[51] In addition to the wide-energy spectra, high-energy-resolution XPS spectra were deconvoluted for O 1s (Fig. 10a–c), Ti 2p (Fig. 10d–f), Mo 3d (Fig. 10g–i), and Si 2p (Fig. 10j and k) to further clarify the oxidation states. The deconvoluted O 1s spectra (Fig. 10a–c) displayed three distinct peaks, representing metal oxides (O-Me), hydroxides (OH^-), and adsorbed water molecules (OH_2). Notably, the 2 wt% Si alloy exhibited a significantly higher metal oxide content (77.07 at%) compared to the 0 wt% Si alloy, which had a metal oxide content of 45.06 at%. This enrichment suggests that the oxide layer on the 2 wt% Si alloy thickened during corrosion, leading to reduced alloy deterioration. Consequently, the passive film on the 2 wt% Si alloy consisted of a dense and compact layer mainly composed

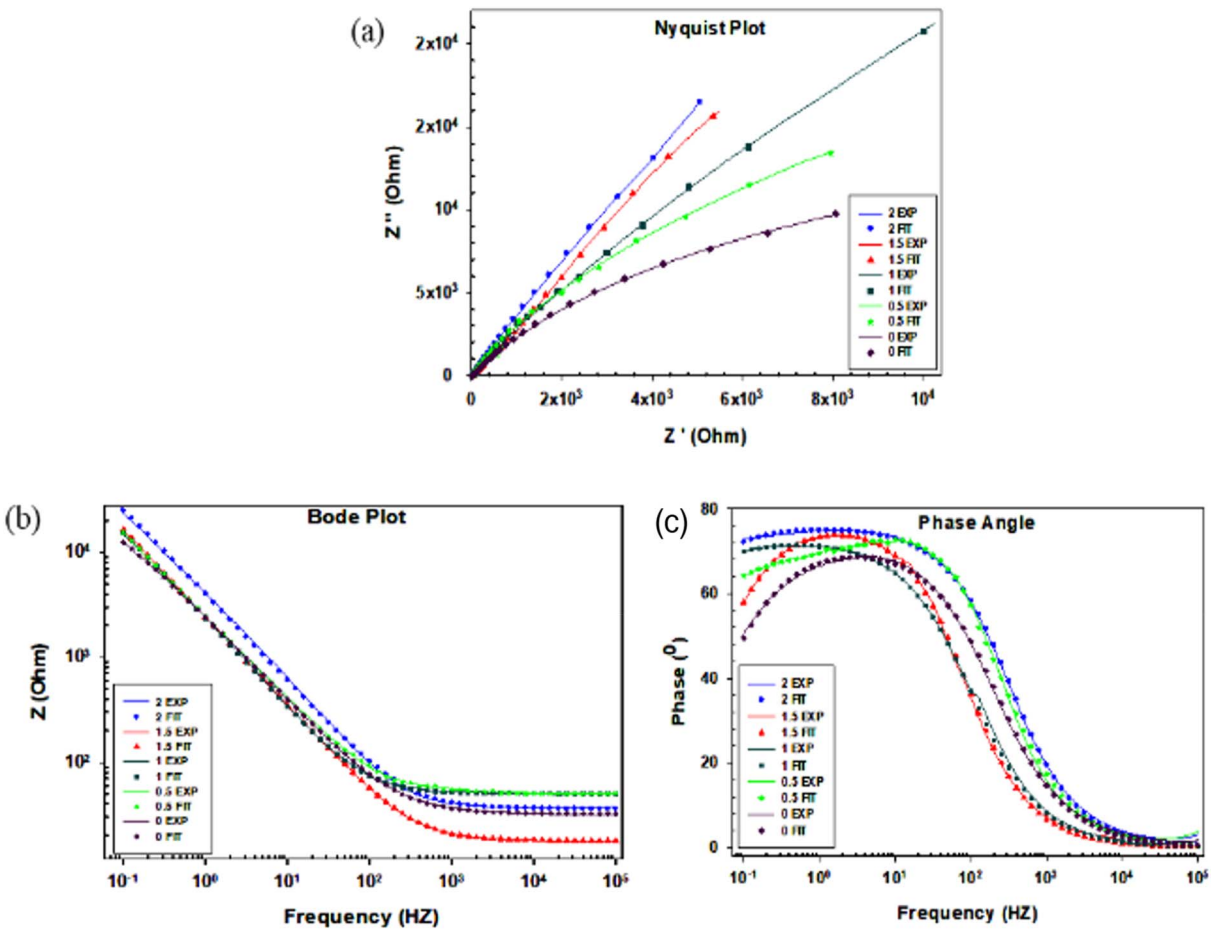

Fig. 8 (a) Nyquist plots, (b) bode magnitude diagrams and (c) bode phase angle diagrams for Ti-15Mo-(*x*)Si alloys ($x = 0, 0.5, 1, 1.5, 2$ wt%) in SBF solution at 37 °C. The symbols correspond to measured data, and the curves represent the corresponding model simulations.

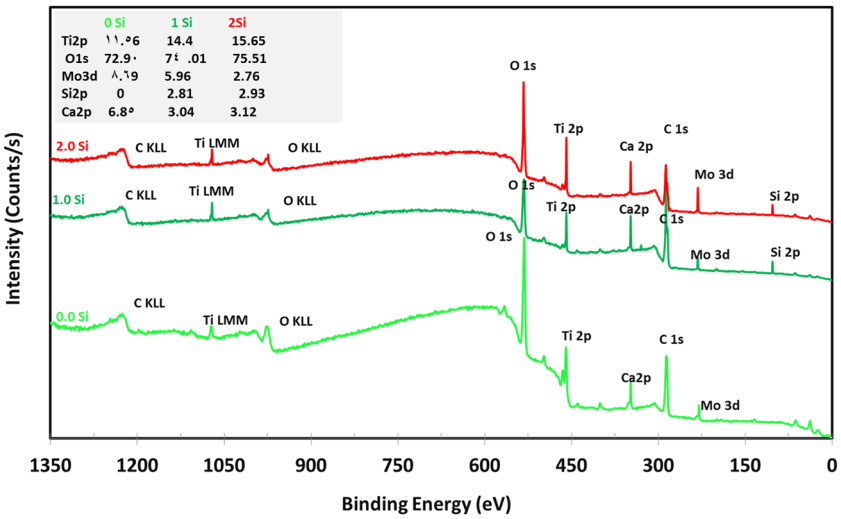

Fig. 9 XPS survey spectra acquired from the corroded surfaces of Ti-Mo-*x*Si alloys (Si = 0, 1, 2 wt%).

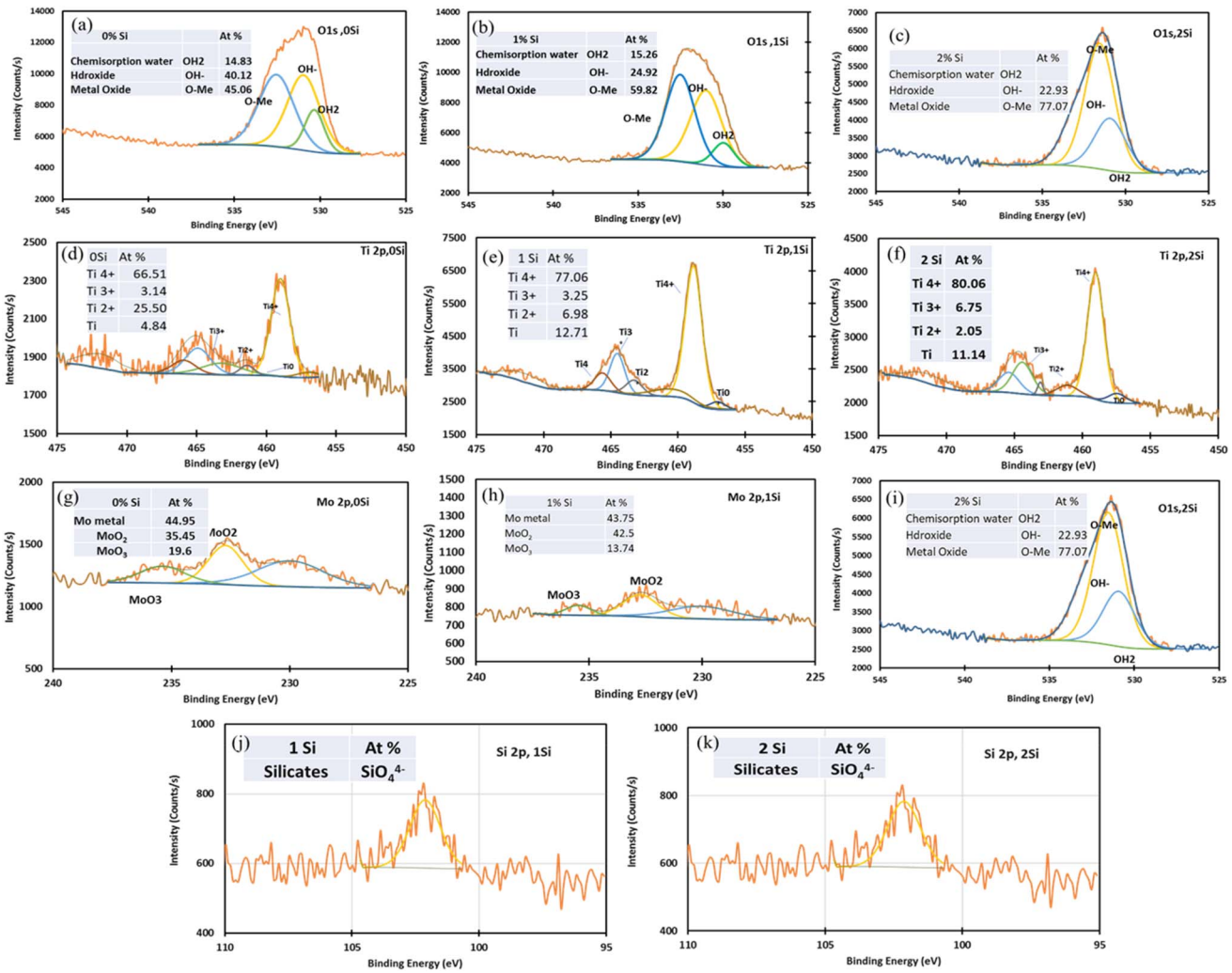

Fig. 10 High-energy-resolution XPS spectra showing the deconvoluted core-level signals for (a–c) O 1s, (d–f) Ti 2p, (g–i) Mo 3d, and (j and k) Si 2p, obtained from the corroded surfaces of the 0, 1, and 2 wt% Si alloys.

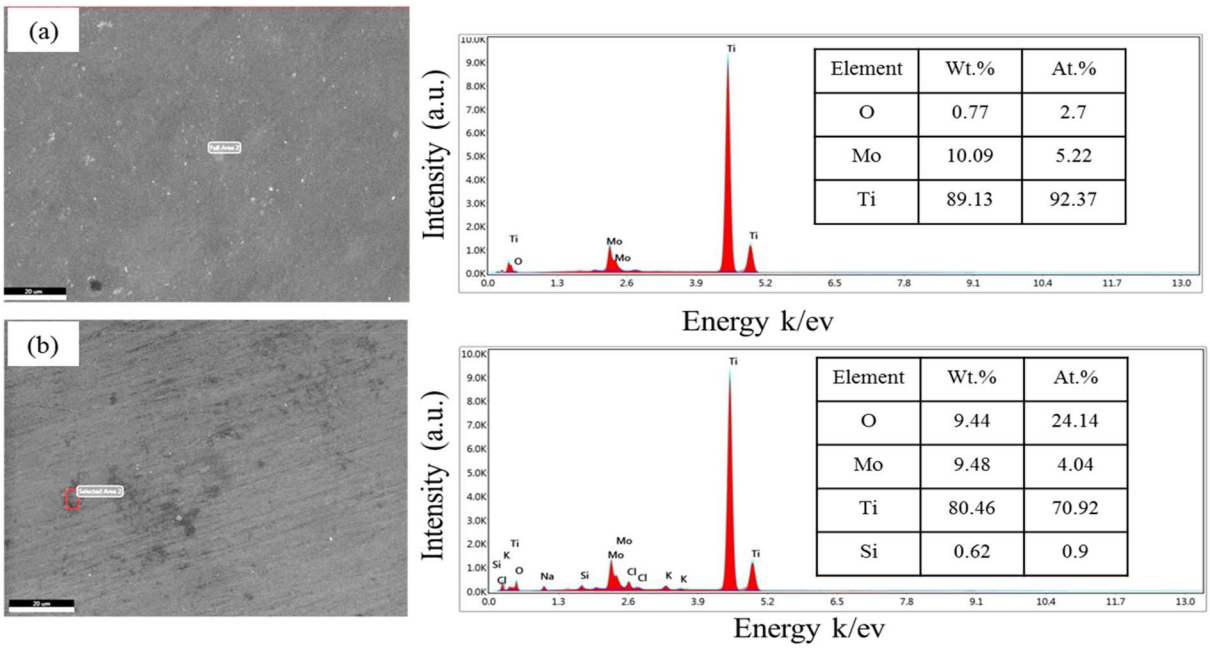

Fig. 11 SEM-EDS micrographs showing the surface morphology of the passive film formed after corrosion testing for (a) Ti-15Mo base alloy and (b) Ti-15Mo-2Si alloy.

of TiO_2, SiO_4^{4-}, and MoO_2, in contrast to the Si-free alloy, which was mainly composed of TiO_2 and MoO_2.

The deconvolution confirms that oxygen is the most abundant element, reflecting the oxide nature of the passive film. Among the detected elements, Ti existed primarily as Ti^{4+} in TiO_2, with minor contributions from lower oxidation states (Ti^{3+} in Ti_2O_3 and Ti^{2+} in TiO). This oxide layer forms as Ti cations diffuse to the surface and react with oxidants (O_2 and H_2O) from the SBF. Furthermore, the analysis reveals that the passive film is a mixed oxide layer, composed mainly of TiO_2, MoO_2, and silicate (SiO_4^{4-}). Weak signals corresponding to MoO_3 were also detected.

These results align with the findings of Rodrigues and Guastaldi;[52] they reported that the passive film on Ti-15Mo alloys is primarily composed of TiO_2 enriched with Mo-based oxides. Also, Biedunkiewicz *et al.*[53] reported the formation of a stable TiO_2 layer doped with Mo on Ti-10Mo and Ti-20Mo alloys, which significantly improves the film's resistance to localized corrosion. The Presence of Mo was detected in the form of Mo, MoO_2, and MoO_3. This multi-oxide composition is further supported by Konatu *et al.*[54] They emphasized the impact of MoO_2 and MoO_3 in enhancing the protective nature of the passive film in Mo-bearing Ti biomaterials.

To further investigate the passive film features, SEM observations were conducted on the corroded surfaces of the Ti-15Mo base alloy and the Ti-15Mo-2Si alloy (Fig. 11). The SEM-micrograph of the Si-free alloy (Fig. 11a) reveals a relatively porous and non-uniform surface layer, which correlates with its lower metal oxide content (45.06 at%) as determined by XPS. In contrast, the surface of the 2 wt% Si alloy (Fig. 11b) appears significantly more compact, dense, and homogeneous. This morphological refinement confirms that the addition of Si, coupled with the formation of mixed oxides (TiO_2, SiO_2 and MoO_x), effectively seals the surface defects and provides a more robust physical barrier against the SBF solution. These visual findings provide a direct confirmation of the XPS results, explaining the enhanced protection and lower corrosion rates observed for the Si-containing alloys.

4 Conclusions

The systematic investigation of the Ti-15Mo-*x*Si alloy system, with silicon additions up to 2 wt%, has yielded significant insights into its microstructural, mechanical, and electrochemical properties, particularly regarding its corrosion behavior in a simulated body fluid (SBF).

1. The incorporation of silicon served as an effective grain refiner, substantially reducing the average grain size. This microstructural refinement directly correlated with a marked improvement in mechanical properties, as evidenced by the increase in both hardness and compressive strength across the compositional series.

2. One of the key findings is the positive role of silicon in improving corrosion resistance. Electrochemical parameters, including open-circuit potential, corrosion current density, and passive film resistance derived from the potentiodynamic polarization and electrochemical impedance spectroscopy measurements, have shown a consistent trend towards improvement with increasing silicon content.

3. All alloys spontaneously formed a stable passive film in the SBF at 37 °C. Silicon systematically improved the corrosion resistance, and the Ti-15Mo-2Si alloy exhibited the most noble open-circuit potential (~−172 mV), the lowest corrosion current

density (~1.03 × 10^{-7} A cm^{-2}), and the highest passive film resistance (~9.58 × 10^5 Ω cm^2).

4. X-ray photoelectron spectroscopy (XPS) analysis revealed that the passive film primarily consists of TiO_2, with contributions from Mo and Si oxides. The film formed on the 2 wt% Si alloy was characterized by a higher proportion of protective metal oxides and a denser, more compact morphology. This superior film quality directly explains the enhanced corrosion resistance observed electrochemically.

5. The synergy of silicon-induced grain refinement and the formation of a robust, silicon-enhanced passive layer provides the Ti-15Mo-2Si alloy with an optimal combination of high strength and exceptional corrosion resistance, making it a highly promising candidate for load-bearing surgical implants. While hardness and compressive strength are critical for such applications, further mechanical characterization (*e.g.*, tensile testing and fatigue behavior) is suggested for future work to provide a more comprehensive evaluation under different loading conditions.

Conflicts of interest

There are no conflicts to declare.

Data availability

The data that supports the findings of this study are available from the corresponding author upon reasonable request.

Funding

This research work was funded by Umm Al-Qura University, Saudi Arabia under grant number: 26UQU4331139GSSR02.

Acknowledgements

The authors extend their appreciation to Umm Al-Qura University, Saudi Arabia for funding this research work through grant number: 26UQU4331139GSSR02.

References

1 G. Senopati, R. A. Rahman Rashid, I. Kartika and S. Palanisamy, Recent Development of Low-Cost β-Ti Alloys for Biomedical Applications: A Review, *Metals*, 2023, **13**(194), 1–31, DOI: 10.3390/met13020194.

2 Y.-L. Zhou and D.-M. Luo, Microstructures and mechanical properties of Ti–Mo alloys cold-rolled and heat treated, *Mater. Charact.*, 2011, **62**(10), 931–937, DOI: 10.1016/j.matchar.2011.07.010.

3 S. Prasad, M. Ehrensberger, M. P. Gibson, H. Kim and E. A. Monaco, Biomaterial properties of titanium in dentistry, *Jpn. J. Oral Biol.*, 2015, **57**(4), 192–199, DOI: 10.1016/j.job.2015.08.001.

4 S. A. Ibrahim, M. M Seleman, H. M. Ahmed and A. E. Hannora, Phase stability of mechanically alloyed Ti-Fe-Al alloys, *IOP Conf. Ser.: Mater. Sci. Eng.*, 2020, **973**, 1–11, DOI: 10.1088/1757-899X/973/1/012025.

5 G. Liu, Y. Yang, X. Luo, B. Huang and P. Li, The phase, morphology and surface characterization of Ti–Mo alloy films prepared by magnetron sputtering, *RSC Adv.*, 2017, **7**, 52595–52603, DOI: 10.1039/C7RA10510J.

6 L. Verestiuc, M. C. Spataru, M. S. Baltatu, M. Butnaru, C. Solcan, A. V. Sandu, I. Voiculescu, V. Geanta and P. Vizureanu, New Ti–Mo–Si materials for bone prosthesis applications, *J. Mech. Behav. Biomed. Mater.*, 2021, **113**, 104198, DOI: 10.1016/j.jmbbm.2020.104198.

7 S. Kumar and T. S. N. S. Narayanan, Corrosion behaviour of Ti–15Mo alloy for dental implant applications, *J. Dent.*, 2008, **36**(7), 500–507, DOI: 10.1016/j.jdent.2008.03.007.

8 N. Ambhore, M. Rajesh and J. E. Manikanta, Recent Advances in Additive Manufacturing for Nanosensors: a Review of Fabrication Techniques, Nanomaterial Integration, and Biomedical applications, *J.Umm. Al-Qura Univ. Eng. Archit.*, 2025, 1–11, DOI: 10.1007/s43995-025-00247-5.

9 E. Ghazanfar, M. A. Marwat, S. A. Batool, M. W. Ullah, K. M. Adam, A. Sajid and R. Areej, Bioactive Ti–3Cu alloys with starch, mesoporous bioactive glass nanoparticles, and clove coating for enhanced orthopedic applications, *RSC Adv.*, 2025, **15**, 47021–47035, DOI: 10.1039/d5ra05140A.

10 N. T. C. Oliveira and A. C. Guastaldi, Electrochemical behavior of Ti–Mo alloys applied as biomaterial, *Corros. Sci.*, 2008, **50**(4), 938–945, DOI: 10.1016/j.corsci.2007.09.009.

11 R. Ramachandran, M. Alsawalha, T. Alomayri, P. Thangavelu, S. Maytasya, A. D. Yunianti and R. S. Alwi, Sustainable fabrication of Ti alloy-coated NiO/Ag bimetallic nanoparticles incorporated with Calotropis gigantea fiber: A dual-purpose material for efficient environmental pollutant degradation and advanced biomedical applications, *Surf. Interfaces*, 2025, **60**, 105995, DOI: 10.1016/j.surfin.2025.105995.

12 W. Abd-Elaziem, M. A. Darwish, A. Hamada and W. M. Daoush, Titanium-Based alloys and composites for orthopedic implants Applications: A comprehensive review, *Mater. Des.*, 2024, **241**, 112850, DOI: 10.1016/j.matdes.2024.112850.

13 C. Sutowo, S. Supriadi, A. W. Pramono and B. Suharno, Microstructure, mechanical properties, and corrosion behavior of new βtype Ti–Mo–Nb based alloys by Mn addition for implant material, *E. Eur. J. Enterprise Technol.*, 2020, **1**, 30–37, DOI: 10.15587/1729-4061.2020.193932.

14 B. S. Sung, T. E. Park and Y. H. Yun, Microstructures and Electrochemical Behavior of Ti-Mo Alloys for Biomaterials, *Adv. Mater. Sci. Eng.*, 2015, 1–7, DOI: 10.1155/2015/872730.

15 F. Xie, X. He, S. Cao, M. Mei and X. Qu, Influence of pore characteristics on microstructure, mechanical properties and corrosion resistance of selective laser sintered porous Ti–Mo alloys for biomedical applications, *Electrochim. Acta*, 2013, **105**, 121–129, DOI: 10.1016/j.electacta.2013.04.105.

16 A. Bakkar, M. M. El-Sayed Seleman, M. M. Zaky Ahmed, S. Harb, S. Goren and E. Howsawi, Recovery of vanadium

and nickel from heavy oil fly ash (HOFA): a critical review, *RSC Adv.*, 2023, **13**, 6327–6345, DOI: 10.1039/d3ra00289f.

17 S. S. Sidhu, H. Singh and M. A. Gepreel, A review on alloy design, biological response, and strengthening of β-titanium alloys as biomaterials, *Mater. Sci. Eng. C*, 2021, **121**, 111661, DOI: 10.1016/j.msec.2020.111661.

18 M. L. Raganya, N. M. Moshokoa, B. Obadele, P. A. Olubambi and R. Machaka, The microstructural and mechanical characterization of the β-type Ti-11.1Mo-10.8Nb alloy for biomedical applications, *IOP Conf. Ser.: Mater. Sci. Eng.*, 2019, **655**, 012025, DOI: 10.1088/1757-899X/655/1/012025.

19 Ș. I. Ghica, V. G. Ghica, M. I. Petrescu, G. Iacob, V. Geantă, M. Buzatu and E. Ungureanu, Design of Ti-Mo-W Alloys and Its Correlation with Corrosion Resistance in Simulated Body Fluid (SBF), *Materials*, 2023, **16**, 2453, DOI: 10.3390/ma16062453.

20 H. Zhao, L. Xie, C. Xin, N. Li, B. Zhao and L. Li, Effect of molybdenum content on corrosion resistance and corrosion behavior of Ti-Mo titanium alloy in hydrochloric acid, *Mater. Today Commun.*, 2023, **34**, 105032, DOI: 10.1016/j.mtcomm.2022.105032.

21 H. W. Hwang, J. H. Park and D. G. Lee, Effect of Molybdenum Content on Microstructure and Mechanical Properties of Ti-Mo-Fe Alloys by Powder Metallurgy, *Appl. Sci.*, 2022, **12**, 7257, DOI: 10.3390/app12147257.

22 W. Xu, M. Chen, X. Lu, D. wei Zhang, H. preet Singh, Y. Jian-shu, Y. Pan, X. hui Qu and C. zong Liu, Effects of Mo content on corrosion and tribocorrosion behaviours of Ti-Mo orthopaedic alloys fabricated by powder metallurgy, *Corros. Sci.*, 2020, **168**, 108557, DOI: 10.1016/j.corsci.2020.108557.

23 Y. Liu, C. Chen, T. Liang, Y. Wang, R. Zhao, G. Li, C. Bai, Y. Wu, F. Yu, L. Sheng, R. Zhang and Y. Zhao, *In vitro* long-term antibacterial performance and mechanism of Zn-doped micro-arc oxidation coatings, *Colloids Surf., B*, 2024, **233**, 113634, DOI: 10.1016/j.colsurfb.2023.113634.

24 W. Ouyang, L. Zhang, H. Wu, D. Wu, S. Zhang, X. Qin, S. Jiang, S. Li, W. Zhang and L. Sheng, Optimized mechanical properties of the hot forged Ti–6Al–4V alloy by regulating multiscale microstructure via laser shock peening, *Int. J. Mach. Tool Manufact.*, 2024, **201**, 104192, DOI: 10.1016/j.ijmachtools.2024.104192.

25 J. Zhang, X. Zhang, H. Wang, M. Wu, X. Ma, X. Liang, J. Zhang, R. Liu, H. Zhao, Z. Sun and J. Zhang, Study on improving the fluidity of Ti2AlNb alloy, *Calphad*, 2023, **83**, 102621, DOI: 10.1016/j.calphad.2023.102621.

26 E. Zhao, S. Sun and Y. Zhang, Recent Advances in Silicon Containing High Temperature Titanium Alloys, *J. Mater. Res. Technol.*, 2021, **14**, 3029–3042, DOI: 10.1016/j.jmrt.2021.08.117.

27 Z. Liu, P. Zhu, X. Mao, Y. Zhao and S. Xin, Effect of Si Addition on the Microstructure and Creep Properties of the Forged Titanium Alloy, *Mater. Chem. Phys.*, 2024, **317**, 129212, DOI: 10.1016/j.matchemphys.2024.129212.

28 D. Qin, Y. Lu, Q. Liu and L. Zhou, Effects of Si Addition on Mechanical Properties of Ti–5Al–5V–5Mo–3Cr Alloy, *Mater. Sci. Eng.*, 2013, **561**, 460–467, DOI: 10.1016/j.msea.2012.10.063.

29 O. Gordillo, W. S. Hincapie, O. Piamba, J. Olaya, J. E. Alfonso, G. Capote and V. Trava-Airoldi, Characterization of Corrosion Products on TiSi, TiAl, and WTi Coatings, *Metals*, 2024, **14**, 1131, DOI: 10.3390/met14101131.

30 Y. Yan, A. Neville and D. Dowson, Biotribocorrosion - An Appraisal of the Time Dependence of Wear and Corrosion Interactions: I. the Role of Corrosion, *J. Phys. D: Appl. Phys.*, 2006, **39**(15), 3200–3205, DOI: 10.1088/0022-3727/39/15/S10.

31 M. A. Hussein, A. S. Mohammed and N. Al-Aqeeli, Wear Characteristics of Metallic Biomaterials: A Review, *Materials*, 2015, **8**, 2749–2768, DOI: 10.3390/ma8052749.

32 L. Kunčická, R. Kocich and T. C. Lowe, Advances in Metals and Alloys for Joint Replacement, *Prog. Mater. Sci.*, 2017, **88**, 232–280, DOI: 10.1016/j.pmatsci.2017.04.002.

33 I. Hulka, J. C. Mirza-Rosca, D. Buzdugan and A. Saceleanu, Microstructure and Mechanical Characteristics of Ti-Ta Alloys before and after NaOH Treatment and Their Behavior in Simulated Body Fluid, *Materials*, 2023, **16**(5), 1943, DOI: 10.3390/ma16051943.

34 W. Xu, X. Lu, L. N. Wang, Z. M., S. M. Shi Lv, M. Qian and X. H. Qu, Mechanical Properties, in Vitro Corrosion Resistance and Biocompatibility of Metal Injection Molded Ti-12Mo Alloy for Dental Applications, *J. Mech. Behav. Biomed. Mater.*, 2018, **88**, 534–547, DOI: 10.1016/j.jmbbm.2018.08.038.

35 Z. Jiang, X. Dai and H. Middleton, Effect of Silicon on Corrosion Resistance of Ti-Si Alloys, *Mater. Sci. Eng. B*, 2011, **176**, 79–86, DOI: 10.1016/j.mseb.2010.09.006.

36 H. A. Aly, M. M. El-Sayed Seleman, A. Bakkar, I. Albaijan, M. M. Z. Ahmed and K. M. Ibrahim, Effect of Si Content on the Thermal Expansion of Ti15Mo(0–2 Si) Biomaterial Alloys during Different Heating Rates, *Materials*, 2023, **16**(13), 4768, DOI: 10.3390/ma16134768.

37 M. M. El-Sayed Seleman, S. Ataya, H. A. Aly, B. Haldar, N. A. Alsaleh, M. M. Z. Ahmed, A. Bakkar and K. M. Ibrahim, Effect of the Si Content on the Dry and Wet Sliding Wear Behavior of the Developed Ti-15Mo-(0-2) Si Alloys for Biomedical Applications, *Metals*, 2023, **13**(11), 1861, DOI: 10.3390/met13111861.

38 A. Terynková, J. Kozlík, K. Bartha, T. Chráska and J. Stráský, Ti-15Mo Alloy Prepared by Cryogenic Milling and Spark Plasma Sintering, *MATEC Web Conf.*, 2020, **321**, 12029, DOI: 10.1051/matecconf/202032112029.

39 A. Gupta, R. K. Khatirkar, A. Kumar and M. S. Parihar, Investigations on the Effect of Heating Temperature and Cooling Rate on Evolution of Microstructure in an α + β Titanium Alloy, *J. Mater. Res.*, 2018, **33**(8), 1–12, DOI: 10.1557/jmr.2018.54.

40 G. Shang, X. Gan, X. Wang, J. Ge, C. Li, Z. Zhu, X. Zhang and K. Zhou, Effect of Cooling Rate on α Variant Selection and Microstructure Evolution in TB17 Titanium Alloy, *Materials*, 2024, **17**(20), 5010, DOI: 10.3390/ma17205010.

41 N. T. C. Oliveira, G. Aleixo, R. Caram and A. C. Guastaldi, Development of Ti-Mo Alloys for Biomedical Applications: Microstructure and Electrochemical Characterization,

Mater. Sci. Eng., 2007, **452–453**, 727–731, DOI: 10.1016/j.msea.2006.11.061.

42 L. C. Zhang and L. Y. A Chen, Review on Biomedical Titanium Alloys: Recent Progress and Prospect, *Adv. Eng. Mater.*, 2019, **21**, 1801215, DOI: 10.1002/adem.201801215.

43 L. Y. Sheng, Y. X. Tian and J. T. Guo, Microstructural Characteristics and Mechanical Properties of a Nb/Nb5Si3 Based Composite with and without Directional Solidification, *Adv. Compos. Lett.*, 2018, **27**(3), 1–8, DOI: 10.1177/096369351802700405.

44 M. P. Alam, M. A. Ali Anshari, M. M. El-Sayed Seleman and M. Imam, Microstructural Tailoring and Property Enhancement via Friction Stir Processing of Additively Manufactured Steel and Ti6Al4V Alloy, *China Weld.*, 2026, **35**(1), 100030, DOI: 10.1016/J.CWE.2026.100030.

45 L. Xu, X. Yu, W. Chen, S. Zhang and J. Qiu, Biocorrosion of Pure and SLA Titanium Surfaces in the Presence of Porphyromonas Gingivalis and Its Effects on Osteoblast Behavior, *RSC Adv.*, 2020, **10**, 8198–8206, DOI: 10.1039/D0RA00154F.

46 M. S. Baltatu, P. Vizureanu, A. V. Sandu, N. Florido-Suarez, M. V. Saceleanu and J. C. Mirza-Rosca, New Titanium Alloys, Promising Materials for Medical Devices, *Materials*, 2021, **14**(20), 5934, DOI: 10.3390/ma14205934.

47 F. Contu, The Cathodic Behavior of Titanium: Serum Effect, *J. Biomed. Mater. Res. B Appl. Biomater.*, 2012, **100B**, 544–552, DOI: 10.1002/jbm.b.31984.

48 J. E. G. González and J. C. Mirza-Rosca, Study of the Corrosion Behavior of Titanium and Some of Its Alloys for Biomedical and Dental Implant Applications, *J. Electroanal. Chem.*, 1999, **471**, 109–115, DOI: 10.1016/S0022-0728(99)00260-0.

49 M. Pankuch, R. Bell and C. A. Melendres, Composition and Structure of the Anodic Films on Titanium in Aqueous Solutions, *Electrochim. Acta*, 1993, **38**, 2777–2779, DOI: 10.1016/0013-4686(93)85098-J.

50 I. C. Lavos-Valereto, S. Wolynec, I. Ramires, A. C. Guastaldi and I. Costa, Electrochemical Impedance Spectroscopy Characterization of Passive Film Formed on Implant Ti–6Al–7Nb Alloy in Hank's Solution, *J. Mater. Sci.: Mater. Med.*, 2004, **15**, 55–59, DOI: 10.1023/B:JMSM.0000010097.86245.74.

51 H. N. Pantaroto, A. B. de Almeida, O. P. Gomes, A. O. Matos, R. Landers, R. C. V. Casarin, J. H. D. da Silva, F. H. Nociti and V. A. R. Barão, Outlining Cell Interaction and Inflammatory Cytokines on UV-Photofunctionalized Mixed-Phase TiO_2 Thin Film, *Mater. Sci. Eng. C*, 2021, **118**, 111438, DOI: 10.1016/J.MSEC.2020.111438.

52 A. Varella Rodrigues and A. Carlos Guastaldi, Ti-Mo Alloys: Corrosion Study in Solutions Simulating Commercial Gels, *J. Polym. Sci. Eng.*, 2018, **1**(1), 897, DOI: 10.24294/jpse.v1i1.897.

53 A. Biedunkiewicz, P. Figiel, D. Garbiec, A. Obrosov, M. Pawlyta, W. Biedunkiewicz, P. Pruss, K. Rokosz and R. S. WróbelRaaen, Influence of Elemental Carbon (EC) Coating Covering Nc-(Ti,Mo)C Particles on the Microstructure and Properties of Titanium Matrix Composites Prepared by Reactive Spark Plasma Sintering, *Materials*, 2021, **14**(1), 231, DOI: 10.3390/ma14010231.

54 R. T. Konatu, D. D. Domingues, R. França and A. P. R. Alves, XPS Characterization of TiO_2 Nanotubes Growth on the Surface of the Ti15Zr15Mo Alloy for Biomedical Applications, *J. Funct. Biomater.*, 2023, **14**(7), 353, DOI: 10.3390/jfb14070353.